Chapter 2

Experimental and Analytical Techniques

In this chapter, sample preparation techniques for both $CuCrO_2$ and $CuFeO_2$ bulk systems are discussed. A brief explanation of various analytical techniques used for understanding the structure, local structure, optical, electrical and magnetic properties of these samples are also been discussed here.

2.1 Sample Preparation

To understand the relation between the electrical and magnetic properties and microstructures of delafossites, various iso-valent and poly-valent doped $CuFeO_2$ and $CuCrO_2$ compounds were prepared. The $CuFeO_2$ compound was partially doped with Ga, Mn, Ti, and V at the Fe site, while the $CuCrO_2$ compound was partially doped with Mg, Ni, Ga, Mn, Ti, Nb, V, and Fe at the Cr site. Such selection of elements is based on the ionic charge, ionic radii and also on the notion that the dopant would favor the valance state whose radii would be close to the parent element radii (Cr^{3+} and Fe^{3+}, respectively).

Two series of samples having the general formula ABO_2 were prepared. Samples of $CuCrO_2$, $CuCr_{0.96}M_{0.03}V_{0.01}O_2$ (M = Ti, Mn, Ga, and Nb), $CuCr_{0.96}V_{0.04}O_2$, $CuCr_{0.97}Mg_{0.03}O_2$, $CuCr_{0.97}Ni_{0.03}O_2$and $CuCr_{1-x}Fe_xO_2$ (x = 0.03, 0.06 and 0.09) were prepared by conventional solid-state technique, while the pure and doped $CuFeO_2$ were prepared through a novel synthesis route involving solid-state technique using high vacuum.

2.1.1 Ceramic Synthesis Route

The solid-state reaction method is the oldest and most simple method which is widely used to fabricate polycrystalline inorganic materials [1]. This method requires the mixing of powdered reactants also may or may not be required to press them into pellets and then high temperature furnace treatment. Also, such reactions become easier if one of the reactants is reactive or which can diffuse easily. Following four things were kept in mind, before planning a solid state reaction:

1. Starting compounds:

The choice of proper starting compounds is very important, their stoichiometry, purity and reactivity should be known with accuracy. Also before the reaction, the raw materials were completely dried and stored in a desiccator.

2. Mixing of raw materials:

In this techniue, it is very important to bring reactant particles in contact, which can be done by increasing the contact surface area. This can be done by mixing or milling the reactants using conventional mortar-pastel (manual method) and/or other labour saving methods like ball milling. The mixing container is properly cleaned so that no contamination takes place. Mixing was done long enough so that the particle size of the reactants is reduced and an intimate mixture is obtained. Also, some time to facilitate the mixing of solvents distilled water or organic liquid like acetone were used and are evaporated at the end of mixing.

3. Heating environment and container:

If the reaction is not sensitive to the atmosphere then the reaction mixture can be heated simply in air in a furnace. But if the reactions are sensitive to the atmosphere these can be heated in an inert surrounding. It can be provided through heating them in presence of inert gases like argon, nitrogen, etc. But it should be noted that the use of these gases requires a lot of care as these methods are expensive and hazardous.

Along with the environment, utmost consideration is to be given to the material of the container, so that it should not react with the raw reactants. For oxides, inert containers that can be used as boats are made of materials like Pt, Au, Al_2O_3, SiO_2, quartz, etc.

4. Heating schedule:

This is not the least, a heating cycle should also be designed in such a manner that:

- Any oxysalt if present should decompose without any melting or leakage from the container.
- Melting and volatilization of the reagent should be avoided, if not then theexcess quantity of salts should be taken to compensate for the losses.
- The reaction normally takes place in an evenhanded time scale (12-24 hrs).

The heating can be done in air or in a controlled atmosphere in tube furnaces. Further, for prevention of the loss of volatile materials, sealed silica tubes or precious metals ampoules can be used.

Based on the above knowledge of the synthesis parameters like sintering temperature, calcination temperature and annealing temperature, time duration of reaction, and reaction environment, reactions conditions were decided for both the series of samples $CuFeO_2$ and $CuCrO_2$. $CuFeO_2$ sample preparation required aninert atmosphere to prevent the conversion of Cu^{1+} to Cu^{2+} ions in these samples, facilitated by gases like nitrogen, argon, etc., which makes the process expensive and hazardous. Here rather than opting for such processes we have chosen to use high vacuum for calcination and annealing purposes, not reported earlier by others as part of the sample preparation technique for these samples [2].

First, the high purity oxides were mixed using mortar-pestle and acetone as awet mixing agent. The powder was dried and then filled into quartz ampoules. These ampoules were evacuated to 2×10^{-5} mbarr and sealed by using an oxy-butane flame. The ampoules were calcined in a muffle furnace at 1273 K temperature for 24 hours and were allowed to cool to room temperature. For homogenization the cycle was repeated two to three times. After the samples were removed and again powdered and compacted to circular discs of 10 mm and squares of 8 mm again filled in the silica ampoules and then evacuated to the same vacuum pressure. The ampoules were given the same cycle two to three times for densification of the pallets.

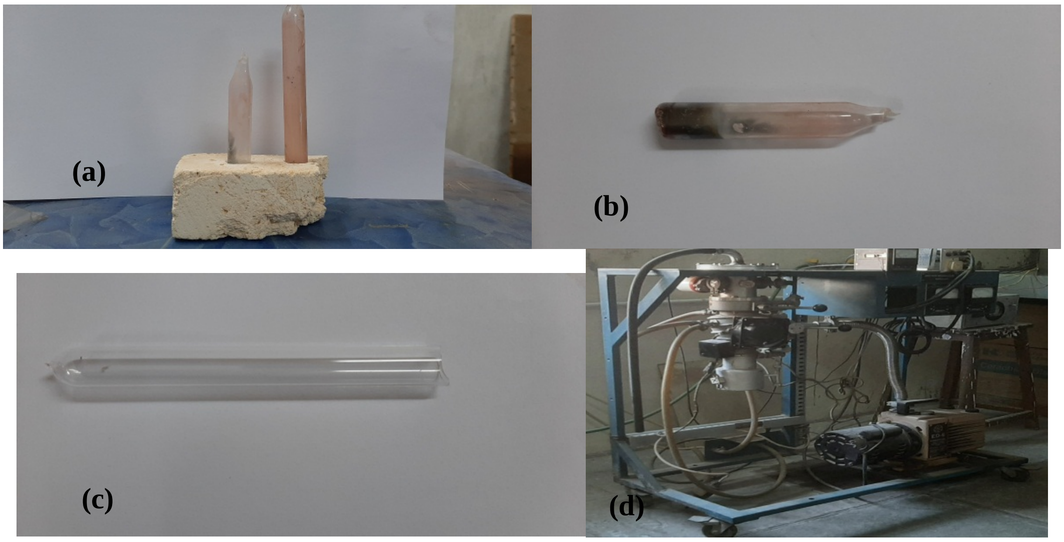

Figure 2.1: (a) Sealed Quartz tube (b) Quartz tube after heating treatment (c) Empty Quartz tube used for heating treatment of raw mixture (d) Vacuum sealing facility a the Department of Physics, Faculty of Sceince, The Maharaja Sayajirao Unicersity of Baroda.

The pure and doped samples of $CuCrO_2$ are prepared by mixing the raw oxide materials using a mortar-pestle for 2 hrs facilitated along with acetone for proper mixing. Also, 1% V has been added to stabilize the phase at lower than the normal sintering temperatures [2]. After mixing the powders the samples were compacted into discs of 12mm diameter by applying 2-ton pressure and calcined at 1100 ^{o}C. As calcined samples were again grinded for homogeneity and circular pallets of 12 mm were prepared by giving 8-ton pressure, which underwent 2 sintering cycles of 24 hrs each.

Table 2. 1: Summary of the prepared samples of both series

Sr. No.	**Sample**	**Formula**	**Formula Mass (g/mol)**	**Calcination (^oC)**	**Sintering (^oC)**	**Duration of Annealing (hours)**
Prepared under High Vacuum						
1.	CFO	$CuFeO_2$	151.385	1000	1000	24
2.	CFMnV	$CuFe_{0.96}Mn_{0.03}V_{0.01}O2$	151.309	1000	1000	24
3.	CFTiV	$CuFe_{0.96}Ti_{0.03}V_{0.01}O_2$	151.098	1000	1000	24
4.	CFGaV	$CuFe_{0.96}Ga_{0.03}V_{0.01}O_2$	151.757	1000	1000	24
5.	CFVO	$CuFe_{0.96}V_{0.04}O_2$	151.189	1000	1000	24
Prepare in air						
1.	CCO	$CuCrO_2$	147.540	1100	1125	24
2.	CCMnV	$CuCr_{0.96}Mn_{0.03}V_{0.01}O_2$	147.618	1100	1125	24
3.	CCGaV	$CuCr_{0.96}Ga_{0.03}V_{0.01}O_2$	148.062	1100	1125	24
4.	CCTiV	$CuCr_{0.96}Ti_{0.03}V_{0.01}O_2$	147.406	1100	1125	24
5.	CCNbV	$CuCr_{0.96}Nb_{0.03}V_{0.01}O_2$	148.757	1100	1125	24
6.	CCVO	$CuCr_{0.96}V_{0.04}O_2$	147.498	1100	1125	24
7.	CCFe-3	$CuCr_{0.97}Fe_{0.03}O_2$	147.656	1100	1125	24
8.	CCFe-6	$CuCr_{0.96}Fe_{0.06}O_2$	147.771	1100	1125	24
9.	CCFe-9	$CuCr_{0.91}Fe_{0.09}O_2$	147.887	1100	1125	24
10.	CCMgO	$CuCr_{0.97}Mg_{0.03}O_2$	146.710	1100	1125	24
11.	CCNiO	$CuCr_{0.97}Ni_{0.03}O_2$	147.741	1100	1125	24

2.2 Characterization Techniques

The requirement and applications of different characterization techniques are presented in this section. The methods of data collection, preparation of the samples and the details of the utilized instruments are briefly mentioned here.

Samples were characterized under three major groupings:

1. Structural Characterization (Crystal structure and microstructure)
2. Molecular Structure
3. Optical and Electrical Properties (optical spectroscopy with electrical transport)
4. Magnetic measurements

2.2.1 Structural Characterization

Structural features of the prepared samples greatly influence the optical, electrical and magnetic properties. Phase purity and structural aspects like grain growth feature importantly influence the overall behavior of the material. Here structural characterizations are carried out using two techniques:

1. X-ray diffraction (XRD) (crystal structure analysis)
2. Scanning electron microscopy (SEM) (Microstructure Analysis)

Also along with XRD Rietveld refinement technique is used here to provide in-depth analysis on Wyckoff's position of the elements, thermal vibrations, space group, etc.

2.2.1.1 X-Ray Diffraction (XRD)

Understanding the properties of materials and tuning them requires the standardization of the material in its pure phase. Also for its industrial application, no impurity phase should be present. There is a characteristic diffraction pattern of any crystalline compound, whether it is present as apure phase or a constituent in a mixture. Using this technique we can confirm - whether the presence of a substance is in the required chemical phase or not. XRD provides information like crystal structure, unit cell parameters, Wyckoff positions of atoms and also the symmetry of the crystal. This information may be used for the simulation of different properties of the materials. Comparing XRD with ordinary techniques of chemical analysis it is much faster, requires asmall quantity of samples and is non-destructive.

X-rays having the wavelength of the order of unit cell dimensions is a very important tool for studying the crystal structure of any material. When a beam of monochromatic X-rays are bombarded on a crystalline material, they get diffracted from the parallel lattice planes, which can be explained by using Bragg’s equation or Bragg’s law [3]:

$$2\mathrm{d}\ \mathrm{Sin}\theta = \mathrm{n}\lambda \qquad (2.1)$$

Where d is the inter-planer spacing, θ is the angle between the incident beam and lattice planes, n is aninteger and λ is the wavelength of the incident X-rays. As per Bragg’s law intensity of the diffracted beam would be maximum, if Bragg’s condition is followed, i.e., the two reflected waves have the path difference equal to the integral multiple of λ (Fig. 2.2).

.

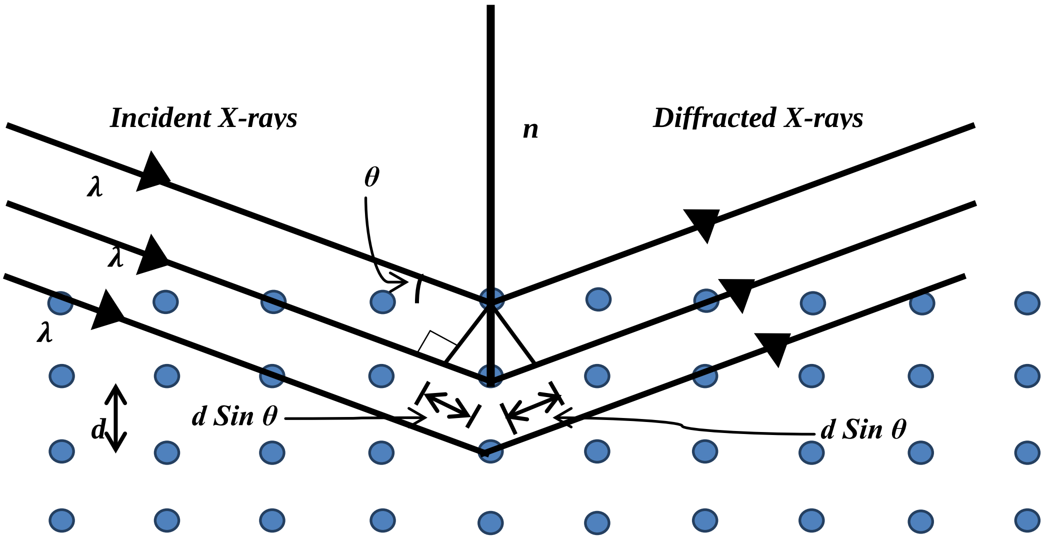

Figure 2.2: Ray diagram depicting Brag's Law

X-ray diffraction studies are useful in finding the:

- d values and hkl values for different sets of parallel planes.
- Unit cell symmetry
- Crystal system and space group
- Lattice parameters
- Wyckoff positions of atoms
- Occupancy of atoms
- Thermal vibrations
- Crystallite size through Debye Scherrer formula [3]
- Crystallite size and induced strain using Williamson-Hall plot [3] and Size-Strain plot method [4].

In our study, X-ray diffraction data of the as prepared powdered samples were studied using **Xpet Pro, Pan Analytical, Singapore**. To collect the XRD data θ-2θ geometry was used along to generate an indirect 2-D image with Cu K_α radiation (1.54 Å). The scanning was performed in the range 2θ = 10-80^o withastep size of 0.02^o. The obtained XRD data were analyzed using the Rietveld refinement technique to further evaluate cell and structural parameters.

Figure 2.3: XRD facility at Department of Metallurgical and Materials Engineering, Faculty of Technology and Engineering, The Maharaja Sayajirao University of Baroda.

2.2.1.2 Rietveld Refinement

Hugo Rietveld developed a technique known as Rietveld refinement for the characterization of any crystalline materials [5]. X-ray and neutron diffraction of powder samples results in characterized peaks in intensity. Using the position, height, and width of the peaks or reflections one can determine structural aspects of any material. In this method, a measured profile is matched and refined with the theoretical line profile using theleast-squares approach. The Rietveld refinement method can be used to refine magnetic and crystal structures from the X-ray diffraction method [5]. WINPLOTR is a graphic program that can graphically display the raw powder diffraction patterns on the computer screen which provides a quick and genuine idea of the quality of the synthesized samples in terms of crystallinity and impurity peaks. Agreement between the calculated data using a particular physical model employed in a specific software and the experimental data is a primary requirement for evaluating the crystal structure of any sample. WINPLOTR can also be used to represent and extract combined plots of as obtained and normalized data files from the Rietveld files produced by refinement program [6] by the modification of the PCR input file, and getting the Reitveld type of plots. Thus, it can be considered as partner software for the refinement Fullprof program [6]

Reitveld analysis of X-ray powder diffraction data can be done using Fullprof program. Profile refinement can be done by creating a PCR file and then modifying it as per requirements in Fullprof program. The format of the input data file must be appropriately given to avoid any error during refinement. The order of the refining parameters is:

- Scale factor
- Zero point for 2θ
- Five of the background parameters
- Cell parameters
- Peak shape parameters
- Z-co-ordinates
- Isotropic displacement parameters
- Occupation numbers
- The fourth peak shape parameter
- background parameter

Other than the above order one can try different routes to get the optimal fitting. Converging to a reliable result is indicated by the R factors. The polycrystalline nature of the sample in majority of the XRD patterns causes overlapping of the Bragg reflections of lower symmetry. Thus as an alternative of looking at the specific reflection or resolving the reflection overlaps, the Rietveld method uses a curve-fitting route by considering the observed intensity y_i(obs) of each alike spaced step Vs calculated Bragg diffraction intensity over the whole pattern comprising the background intensity and the sum of the contribution of reflections close to the i^{th} powder pattern step:

$$y_i\,(obs) = y_i(background) + \Sigma\, y_i(Bragg) \qquad (2.2)$$

By using the plot of the difference between the calculated and observed patterns one estimates the fitting results. Also, there are other numerical terms that can be used to determine the goodness of the least square refinements as below [7]:

R-pattern $$R_p = \frac{\Sigma|Y_{i(obs)} - Y_{i(calc)}|}{\Sigma Y_{i(obs)}} \qquad (2.3)$$

R-weight pattern $$R_{wp} = \left|\frac{\Sigma w_i (Y_{i(obs)} - Y_{i(calc)})^2}{\Sigma w (Y_{i(obs)})^2}\right|^{1/2} \qquad (2.4)$$

Where $Y_{i(obs)}$= observed intensity at angular step i , $Y_{i(calc)}$ = corresponding calculated intensity and w_i = weight function

Bragg factor $R_{Bragg} = \frac{\Sigma_j |I_{jo} - I_{jc}|}{\Sigma_j I_{jc}}$ (2.5)

I_{jo} = observed integrated intensities and I_{jc} = calculated integrated intensities for the different Bragg peaks j.

Goodness of fit $\chi^2 = \left[\frac{R_P}{R_{wp}}\right]^2$ (2.6)

2.2.1.3 Scanning Electron Microscopy (SEM)

Thescanning electron microscope uses the sample-electron interaction to reveal information like morphology, chemical composition, crystal structure and orientation of the samples studied. For collecting data, a particular area of the sample is scanned and a 2-D image is generated which shows the properties of the sample. Magnification of any object up to approximately 300000x can be achieved with the resolution of **a** few nanometers.

SEM uses ahigh-energy focused beam of electrons to generate the indirect 2-D image of the samples Fig. 2.4. A significant amount of energy carried by accelerated electrons on interaction with the solid sample produces avariety of signals like backscattered electrons, secondary electrons, diffracted backscattered electrons, photons (characteristic X-rays), visible light and heat. The morphology and topography of the sample are shown by the secondary electrons and backscattered electrons. Inelastic collisions of the bombarded electrons with the electrons in the discrete shells of the atoms produce characteristic X-rays of the particular element present in the sample. There is no loss in the volume of the sample due to the interaction of the incident electrons with elemental electrons, thus the same sample can be studied repeatedly. Thus, SEM is a non-destructive analysis technique.

Samples of metals, ceramics, dust, hair, teeth, bones, wood, ceramics, polymers, etc., can be studied using SEM.

In the present study, the microstructure photographs of the annealed bulk samples were collected using **Model S 3400 N, Hitachi at Labzone services, Powai Mumbai.** Different magnifications were used to study the growth features. The sample surfaces were coated with silver to eliminate any electron charging effect.

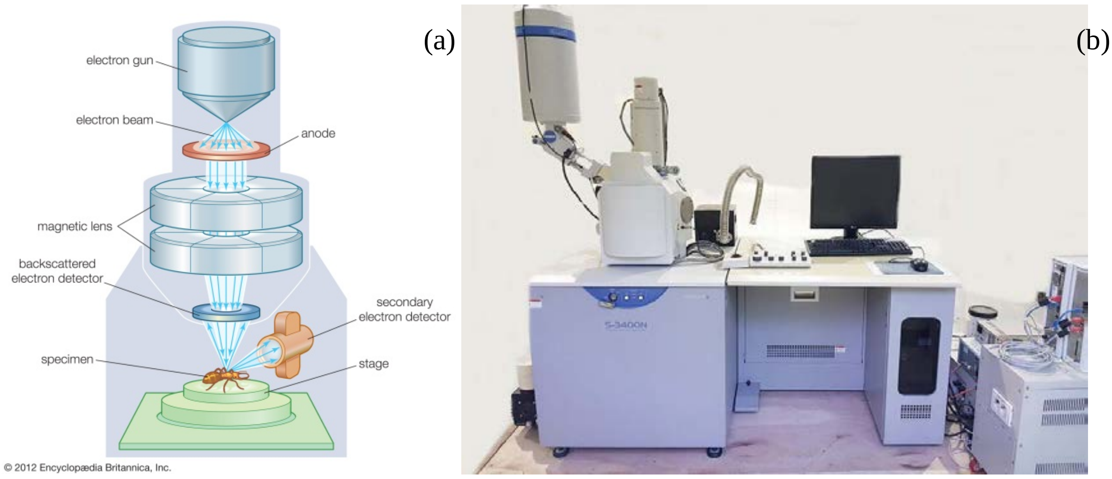

Figure 2.4: (a) Schematic diagram of Scanning electron microscope [8] (b) SEM instrument Model S 3400 N by Hitachi

2.2.2 Molecular structure studies

Infrared absorption and Raman scattering are the major techniques that are used to detect themolecular vibrations. These techniques help to identify the substances using their characteristics spectral shapes (‘fingerprinting’) and to quantitatively or semi-quantitatively find the amount of substance present in a sample. Samples can be examined as solids, liquids or vapors, surfaces or bulk. A variety of interesting and challenging problems can be solved using these techniques. The recent advances in technology have made itpossible to study the samples in glass containers and unprepared samples.

2.2.2.1 Raman spectroscopy

Inelastic scattering of light was first hypothesized by Smekal in 1923 [9]. Also, actual experimental observation for the first time was studied by Raman and Krishnan in 1928 [10]. The photons of light may get absorbed or scattered or even pass unaffected on interaction with matter. If the photons of certain energy get absorbed by the molecule and result in excitation to higher energy levels, resultant changes are measured through absorption spectroscopy. However, in thecase of photon scattering, there is no need for the incident photon to have energy equal to the difference between two molecular energy levels. The scattered photons can be observed at an angle θ from the incident photons and studied. This technique is widely used inanalytical methods for measuring the particle size and distribution of particle sizes down to 1 μm.

In Raman spectroscopy, the objective of radiation is different**.** Here radiation having a single wavelength is used to irradiate the sample and the scattered radiation having one vibrational unit of energy difference ro that of the one incident is detected. Thus, matching of incident energy with the difference in theground and excited state of the molecule is not required. Here polarization of the electron cloud around the nuclei takes place on the interaction of the molecule with the incident radiation. This produces a short-lived state called ‘virtual state’, which is unstable and the photon is quickly re-radiated.

In vibrational spectroscopy, the energy changes that are detected are due to nuclear motion. On scattering, if only electron cloud distortion occurs it will cause very small frequency changes in scattered photons, as electrons are very light. This is elastic scattering also known as Rayleigh scattering for molecules. But if induction of nuclear motion occurs while scattering, then the energy may be transferred from incident radiation to molecule and vice versa. The nature of such interaction is inelastic and adifference in energy is observed in the scattered photon in comparision to the incident photon by one vibrational unit. This phenomenon is called Raman scattering [11]. One in 10^6 - 10^8 photons will beRaman scattered.

Basic phenomena occurring for one vibration are shown in figure 2.5. Most of the molecules are present at thelowest energy vibrational levels at room temperature. As the virtual states of the molecules are created by the polarization of electron clouds due to interaction with laser, their energy is determined by the frequency of light source used. As the Raman scattering is very less Rayleigh would be the dominant process. Stokes scattering arises because of absorption of energy by the molecule due to thescattering process from the ground vibrational state ‘*a*’ to a higher energy excited vibrational state ‘*b*’ (figure 2.5). On the other hand, some of the molecules may already be present in the excited state ‘*b’* and they may transfer the energy to the scattered photon to come to the ground vibrational state ‘*a*’ (figure. 2.5). Depending on the population of various energy levels, one can observe the relative intensities of the two states. Also, at room temperature, the number of molecules in the excited energy state is expected to be low. This will result inweak anti-Stokes scattering compared to Stokes scattering as the frequency of vibration increases.

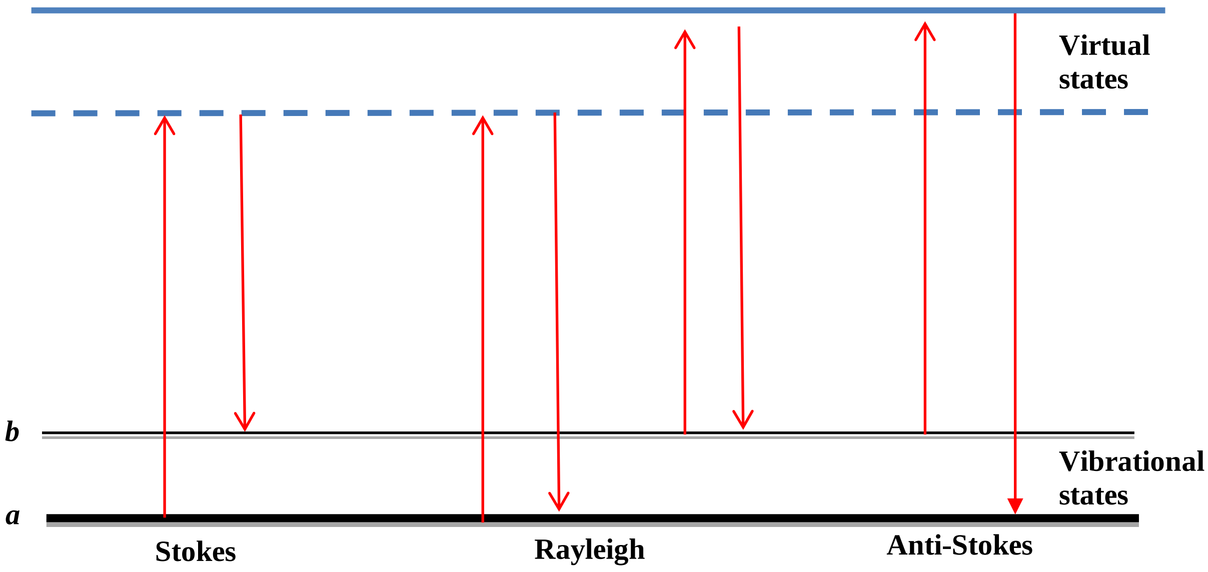

Figure 2.5: Rayleigh and Raman scattering process

The majority of measurements are analyzed using the Stokes lines. But in rare cases, anti-Stokes lines which are very weak are used, where fluorescence interference occurs at alower energy than the excitation frequency.

In the present study**,** the Raman spectra of the samples were collected at room temperature using a**micro Raman model comprising Peltier cooled CCD detector equipped with Nikon microscope of different objective lenses and Nd-YAG laser source having 532 nm wavelength. This Facility is present at the Faculty of Science, Maharaja Sayajirao University of Baroda.**

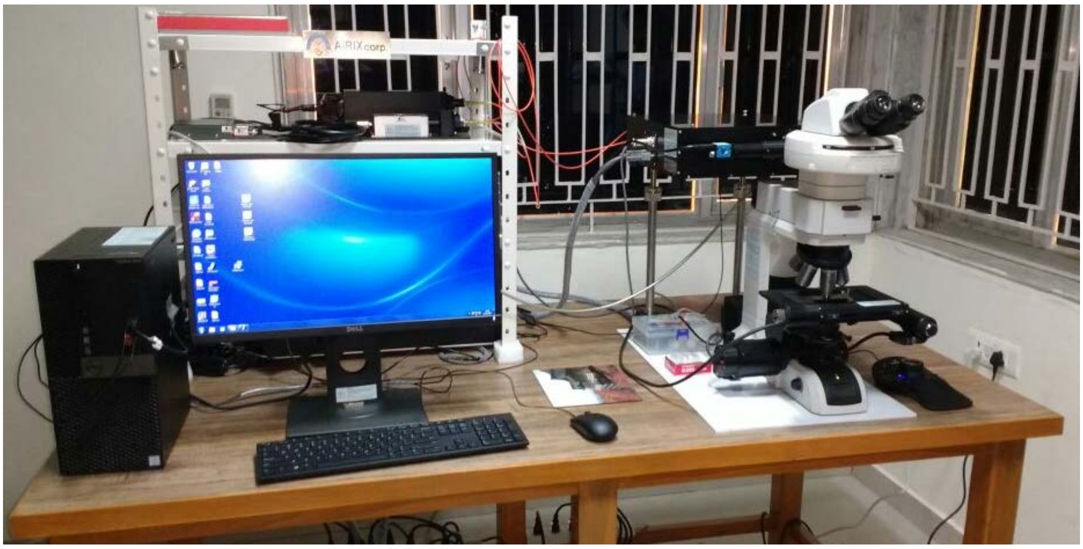

Figure 2.6: Raman Facility at Department of Physics, Faculty of Science, The Maharaja Sayajirao University of Baroda.

2.2.2.2 Infrared Spectroscopy

Unlike the Raman technique, the absorption process is used ina wide range of spectroscopic methods. Acoustic spectroscopy is the process where there is a very small difference in the ground and state, while in the case of X-ray absorption spectroscopy there is a large difference between the two. In between the two limits, there are techniques like infrared absorption spectroscopy.

A range of frequencies is bombarded on the sample in case of infrared spectroscopy and where there is a match in the vibration energies the incident radiation is absorbed and the molecule is stimulated to a vibrationally excited state. This loss in frequency is detected.

Infrared absorption is shown by a molecule when its electric dipole moment changes during the vibration, which is a selection rule for this spectroscopy. When a bond expands or contracts the dipole moment changes. It happens when the bond is between two different atoms, while in the case of thehomo nuclear bond the dipole moment is zero irrespective of the bond length. Thus, molecules having permanent dipole moments are only capable of absorbing infrared radiations [12].

A bond has a natural frequency of vibration and thesame bond in two different molecules having different environments results in the different characteristic infrared spectrum. Therefore this technique can be effectively used to identify different materials. Also, the peak size in the spectrum points to the amount of material present [13].

This technique is non-destructive, has greater optical throughput, high speed of collecting data, is accurate without the need of external calibration and hashigher sensitivity. The limitations of the dispersive instruments like slow scanning and measurements of all infrared frequencies led to the development of FT-IR spectroscopy. In this method, an optical device which is the interferometer was developed to overcome such limitations. This makes the measurements quick. An interferogram is produced by the interferometers which is the combination of thetwo-beam signal. Direct interpretation of the interferogram is not possible and its decoding is required by a technique called the Fourier transformation, which is performed by the computer. This produces thedesired spectrum which can be used for the analysis [13].

The FT-IR instrument involves the source, the interferometer, sample, the detector and the computer. The schematic representation is shown in the figure below.

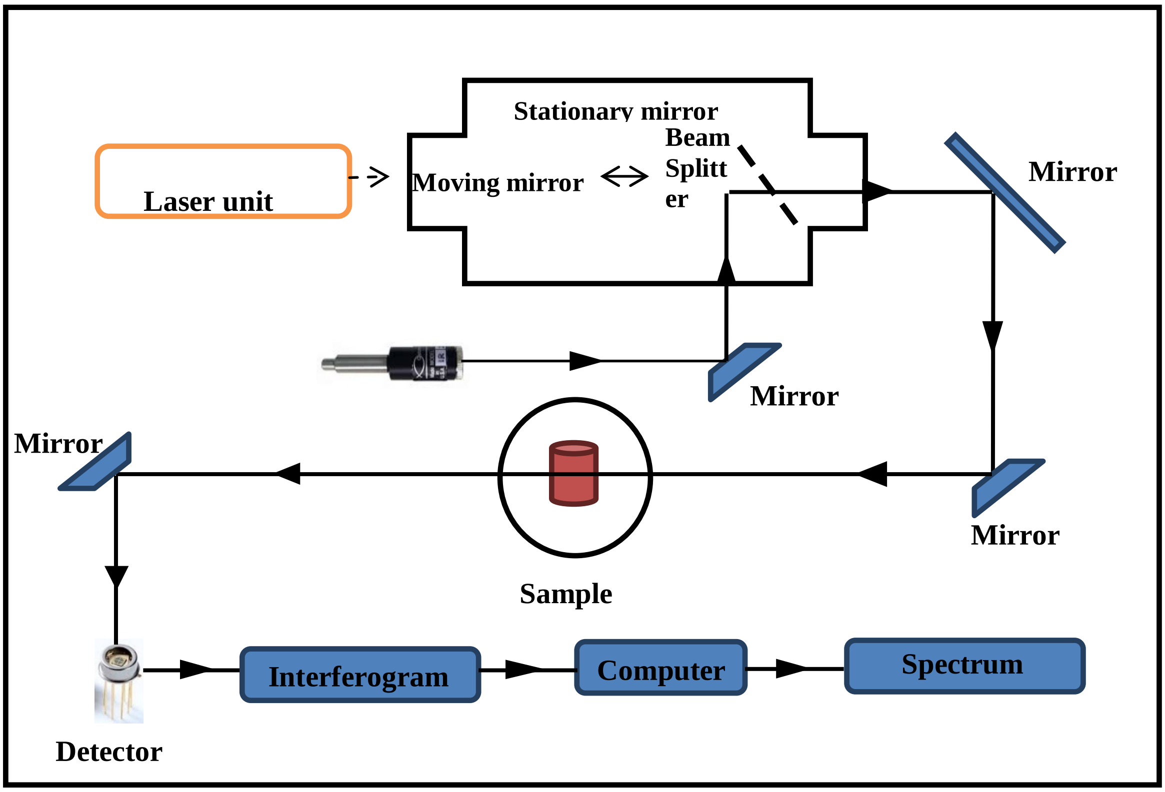

Figure 2.7: Infrared Spectrometer Schematic Diagram

A background spectrum needs to be measured which nullifies the effect related to the instrument. A background spectrum is collected usually without any sample. This process confirms the spectrum obtained has all features related to sample only.

A background spectrum needs to be measured which nullifies the effect related to the instrument. A background spectrum is collected usually without any sample. This process confirms the spectrum obtained has all features related to thesample only.

In the present study, the room temperature FTIR spectra of the samples were collected using **FTIR-8400S by Shimadzu, at the Department of Applied Chemistry, Faculty of Technology and Engineering, The Maharaja Sayajirao University of Baroda**.

Figure 2.8: Infrared Spectrometer at Dpeartment of Applied Chemistry, Faculty of Teechnology and Engineering, The Maharaja Sayajirao University of Baroda.

2.2.2.3 Mössbauer Spectroscopy

Mössbauer Effect is a process of recoil-free emission and nuclear transitions resulting in gamma emission without the loss of energy [14]. This phenomenon is named after Rudolf Mössbauer, who observed this effect in 1957 and received the Nobel prize in 1961.

Mössbauer Effect in combination with the Doppler Effect is used to identify the hyperfine transitions between the excited and the ground state of the nucleus. This is commonly studied through ^{57}Fe isotope. No external field is required and very weak magnetic interactions can be studied even without perturbing the effect of external magnetic fields [15], [16]. In the Mössbauer Effect,the recoil energy depends inversely on the mass of the system. As the solid is heavier, it absorbs the energy as phonon but there is a probability that no phonons or a recoilless emission of gamma rays take place.

In this technique, a source of ^{57}Co nuclei provides a healthy supply of excited ^{57}Fe nuclei, whose decay to theground state is supplemented by a gamma-ray emission. When the energy level of the absorbing nuclei resonantly matches with the emitted gamma-ray, thetransition occurs through the absorption. For the above process, the source is moved toward and away from the absorber (sample) in an oscillating manner usually at a velocity of few mm/s to provide aDoppler shift. A Mossbauer spectrum contains combined effects of hyperfine interactions: isomer shift, quadrupole interactions and magnetic splitting, which helps in probing the structural elements of the nucleus.

Isomer Shift:

It occurs when the source and absorber are different, i.e. their nuclear radius, electron density and as a result the energy difference isnot the same for the two species defined as due to Coulombic interaction effects. This is given by the equation [17]:

$$\delta = E_A - E_S = \frac{2}{3} nZe^2(\rho_A - \rho_S)(R_{es}^2 - R_{gs}^2) \qquad (2.7)$$

Where δ = energy change necessary to excite the absorber seen as a shift from the Doppler speed 0 to V_1, ρ_A and ρ_S are the electron densities of the absorber and the source, R_{es} and R_{gs} are the radii of the nuclei at excited and ground state. The Isomer shift directly depends on the s-electrons and may be influenced by the shielding electrons of p, d, f orbitals**.** This can be used to identify the valance state of absorbing atom or charge transfer, also lattice expansion or compression as well as changes in the electron density [17].

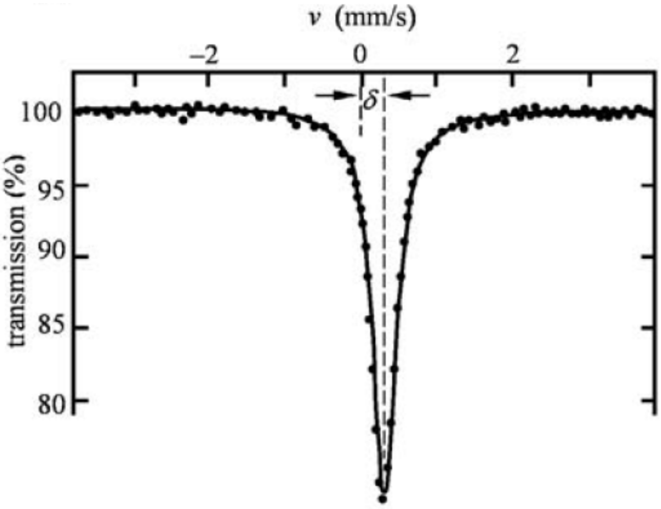

Figure 2.9: A typical isomer shift present in a Mössbauer spectrum [18]

Quadrupole Splitting:

Quadrupole splitting arises due to a non-spherical charge distribution present in the nuclei in states with an angular momentum quantum number I > 1/2. When subjected to an asymmetrical electric field which is produced by an asymmetric ligand arrangement or electronic charge distribution splits the nuclear energy levels. Such charge distribution is characterized by ‘Electric Field Gradient’.

In thecase of ^{57}Fe or ^{119}Sn with excited state I= 3/2, splits into two sub-states $m_l = \pm1/2$ and $m_l = \pm3/2$, giving a doublet or two-line spectrum [19].

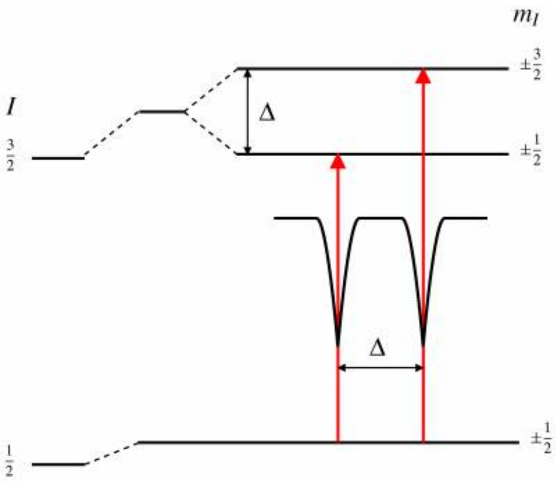

Figure 2.10: Typical quadrupole splitting. 'Δ' gives the magnitude of quadrupole splitting [20]

This helps in understanding the local surrounding of the Mossbauer atom and valence electron configuration.

Magnetic Splitting:

Magnetic splitting is observed due to the interaction of the nuclear spin moment with the dipolar interaction of the magnetic field. The effective magnetic field of the nucleus is due to many sources, i.e. $B_{eff} = B_{cont} + B_{orb.} + B_{dip.} + B_{app}$[21]–[26]. $B_{cont.}$ arises because of the spin of those electrons polarizing the nuclear spin density. $B_{orb.}$ is a result of theorbital moment of those electrons while, $B_{dip.}$ is the dipolar field arising out of the spin of those electrons. Thus the first three terms are due to partially filled electron shells of the atom itself.

A typical magnetic splitting for ^{57}Fe is shown in the figure below. Six possible transitions for a 3/2 to 1/2 transition give rise to a sextet, with line spacing proportional to the effective magnetic field.

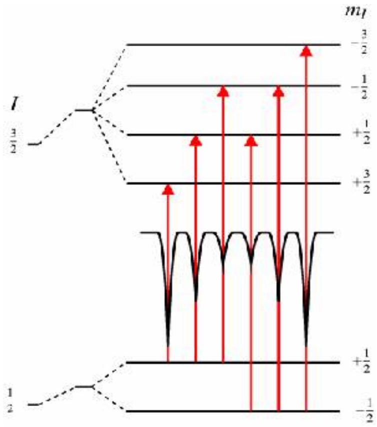

Figure 2.11: A typeical magnetic splitting of nuclear energy levels[20]

This effect is helpful in understanding the magnetic exchange interactions and local magnetic field [27]. In the present study, bulk powder samples of the pure and doped $CuFeO_2$ we used as absorbers for room temperature measurements. **A Mossbauer constant acceleration spectrometer whole line width was 0.22 m/s was used. A source of ^{57}Fe in Rh matrix was used. This facility is present at the UGC-DAE Consortium for Scientific Research, Indore Center**.

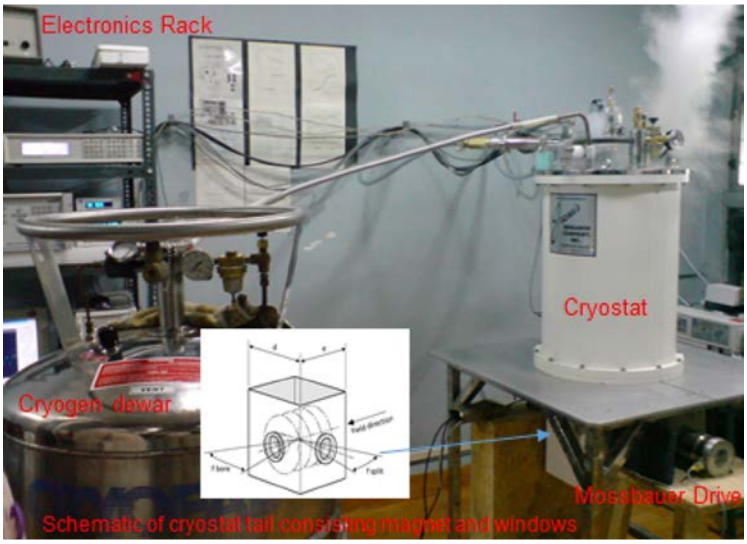

Figure 2.12: A typeical magnetic splitting of nuclear energy levels[28]

2.2.3 Optical, Electrical resistivity and Dielectric properties

Intrinsic as well as extrinsic properties of the material decide its electrical properties. The intrinsic parameters significantly affect the optical and electrical properties of the materials i.e. properties like-charged states of constituent ions, atomic positions**,** charge center symmetry, the electronegativity of the ions, etc. Such parameters are explained by research groups in relation totilting of oxygen octahedron, frequency and temperature-related dipole relaxations, structural distortions [29]–[33]. Also, extrinsic parameters like oxygen vacancies, defects, etc., affect optical and electrical properties [34]–[37]. The optical spectroscopy along with the electrical studies provides information about the contributing factors in a satisfactory manner. The optical and the electrical measurements can be performed using thefollowing methods:

1. UV-Visible Diffuse Reflectance spectroscopy
2. Electrical resistivity measurement
3. Dielectric Measurement

2.2.3.1 UV-Visible Diffuse Reflectance spectroscopy (DRS)

Semiconductors have an important feature which is its energy gap (E_g) that determines its optoelectronic applications [38]–[41]. For thin films, UV-Visible absorption spectroscopy is mostly used as the scattering is low in films [42]. Most of the time it is common to come across powdered samples in place of thin films or colloids and normally for UV-Vis absorption spectroscopy sample is dispersed in liquid media like water, alcohol, etc. for measurement purposes. In powder samples sometimes the particle size of the samples is not small enough to disperse in the liquid. Thus, to avoid such problems DRS technique is used where the materials are unsupported [43].

Uneven or granular surface causes diffuse reflection of light where the incident ray is seemingly reflected at several angles. These kinds of reflection do not follow Snell’s law for a plane mirror-like reflection. The radiation travesesinto the interior of the solid and after multiple scattering emerges fromto the surface causing diffuse reflectance. There are several modelsproposed to designate diffuse reflectance phenomenadepending on the optical properties of the material. Kubelka and Munk proposed a model which makes it possible to use diffuse reflectance spectra [44]. Kubelka-Munk's theory is based on the behavior of light traveling inside a light-scattering specimen. Following are the differential equations on which it is based:

$$-\mathrm{di} = -(\mathrm{S}+\mathrm{K})\mathrm{idx} + \mathrm{Sjdx} \qquad (2.8)$$

$$-\mathrm{di} = -(\mathrm{S}+\mathrm{K})\mathrm{jdx} + \mathrm{Sidx} \qquad (2.9)$$

The intensities of light travelingtowards the un-illuminated and illuminated surfaces of the samples isgiven by i and j, respectively. The differential segment along the light path is given by *dx*, *S* and *K* are the K-M scattering and absorption coefficients respectively. S and K have no direct physical meaning but are supposed to represent the parts of light scattered and absorbed respectively, per unit vertical length [45].

Thickness and sample holder do not influence the value of reflectance (R), in the case of an infinitely thick sample. In such **a** situation the K-M equation becomes:

$$\frac{K}{S} = \frac{(1-R_\infty)^2}{2R_\infty} = F(R_\infty) \qquad (2.10)$$

Here $F(R_\infty)$ is called the K-M function, here $R_\infty = R_{sample} / R_{standard}$ [46].

The bandgap E_g, and absorption coefficient α is given of a direct bandgap semiconductor in a parabolic band structure is given by the well know relation [47]:

$$\alpha h\nu = C_1(h\nu - E_g)^{1/2} \qquad (2.11)$$

Where α =linear absorption coefficient, hν = photon energy, and C_1 = proportionality constant. K-M absorption coefficient $K = 2\alpha$ where the material scatters in **a** perfectly diffuse manner. K-M coefficient S is considered constant in this case with respect to wavelength. Using the remission function in Eq. (2.11) we obtain the equation:

$$[F(R_\infty)h\nu]^2 = C_2(h\nu - E_g) \qquad (2.12)$$

Thus plotting $[F(R_\infty)h\nu]^2$against hν, the bandgap of a powder sample can be obtained.

DRS wasperformed using **Perkin Elmer, USA, and model: Lamda 950 at UGC-DAE-CSR, Indore center**. It is a double beam, double monochromator ratio recording spectrometer, having a wavelength bounds of 175 nm to 3300 nm, resolution of 0.05 nm and accuracy of wavelength was ± 0.08 nm.

Figure 2.13: UV-Vis spectrometer facility at UGC-DAE-CSR, Indore Center

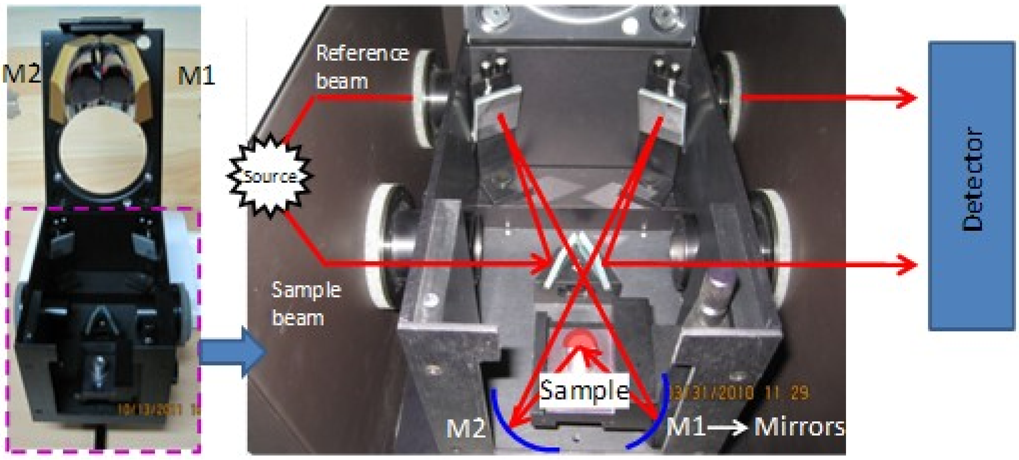

Figure 2.14: Attachments for the UV-Vis Spectroscopy for Diffuse reflectance mode at UGS-DAE-CSR, Indore center.

2.2.3.2 DC Electrical Resistivity Measurement

This is a straightforward and simple method that furnishes much useful information about the sample. Electrical resistivity measurement with respect to temperature provides evidence regarding the temperature-dependent electronic phase transitions. In our study, we have used a standard four-probe technique to measure electrical resistivity as a function of temperature. Low contact resistance is required for such measurements [48], [49]. Thus electrical contacts are made using silver paste as shown in Fig. 2.15 below. All this assembly is kept on to a sample holder and the wires are connected to the measuring instruments using leads.

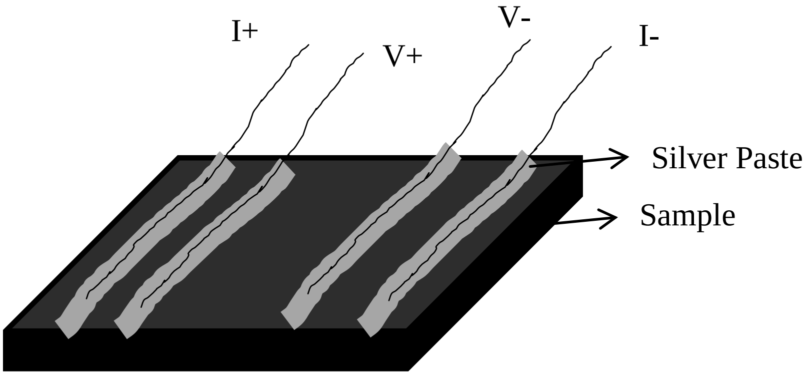

Figure 2.15: Representative diagram of the Four probe contacts for current and voltage supplies to the sample

Resistivity measurements in the present study weredone by passing a constant current through the current terminals using **Keithley's constant current source (Model 6221)** and the voltage was measured using **Keithley Nanovoltmeter (model 2182A)**. Temperature-dependent measurement was done using a closed cycle refrigerator (CCR). The resistance is calculated following Ohm’s Law $V = IR$, where V is the voltage developed and I is the current passed. The electrical resistivity can be calculated using the formula:

$$\rho = \frac{\mathrm{RA}}{\mathrm{L}} \qquad (2.13)$$

Here R is the resistance, L is the length, A is the area of thecross section of the sample. Samples were cooled using liquid helium and measurements were done during the warming cycle. Figure 2.15 below shows the **low-temperature resistivity measurement facility at MIT, MAHE, Manipal**, where the measurements were performed.

Figure 2.16: Low temperature resistivity setup at MIT, MAHE, Manipal

2.2.3.3 Dielectric Measurements

Now a days a lot of importance is given to the measurement of complex dielectric properties of the materials in the research fields of material science, microwave circuit design, biological research, etc. Such a measurement is important as it has proved very useful in the field of research and development.

Dielectric property involves the measurement of the complex relative permittivity (ε_r), which consists of thereal part and an imaginary part. The real part is also known as the dielectric constant which is a measure of the amount of energy that can be stored in the material from the external electrical field. The imaginary part is called the loss factor and is zero for lossless materials. It is the measure of the amount of energy lost by the material due to an external field. There is also a term called loss tangent denoted by *'tan δ'* which is the ratio of the imaginary part to the real part of ε_r. The loss tangent is also known by the terms dissipation factor or loss factor.

In this measurement**,** the choice of the proper electrode is very important. In our measurements, circular pallets of suitable diameter and thickness were prepared whose surface was properly polished and silver paste was applied to make proper contacts. This type of electrode was adopted as (i) it reduces the error in the measurement to the minimum due to the air gap between the electrode and sample surface, and (ii) this method of measurement is relatively very simple compared to other non-contact methods. Such dielectric setup provides information about the behavior of the dielectric constant of materials such as magnetic, multiferroic and ferroelectric materials.

In the present study,the dielectric constant of the samples was calculated by measuring the capacitance of the samples. Low-temperature dielectric measurements were performed using a **Novocontrol Alpha Impedance analyzer having a He-gas exchange attachment along with a closed-cycle refrigerator**. The capacitance data were collected within the frequency range of 1 Hz – 1 MHz. The temperature range was 5-300 k and the heating rate was kept at 0.8 K/min. Thedielectric measurement setup is shown in the figure below.

Figure 2.17: Dielectric measurement facility at Solid State Physics Division, Bhabha Atomic Research Centre, Trombay.

The standard relations along with sample dimesions used for converting impedance data in to complex permittivity data are as follows:

$$\varepsilon^{*} = \varepsilon^{'} + i\varepsilon^{''} \qquad (2.14)$$

$$\varepsilon^{'} = \frac{-d}{\omega\varepsilon_{o}A}\frac{Z^{''}}{(Z'^{2}+Z''^{2})} \qquad (2.15)$$

$$\varepsilon^{''} = \frac{-d}{\omega\varepsilon_{o}A}\frac{Z^{'}}{(Z'^{2}+Z''^{2})} \qquad (2.16)$$

$\mathcal{E}_0$ = permittivity of vacuum

$\mathcal{E}^{'}$ = real part of dielectric constant

$\mathcal{E}^{''}$ = imaginary part of dielectric constant

$Z^{'}$ = real part of impedance data

$Z^{''}$ = Imaginary part of dielectric constant

A = area of electrode

d = separation between electrodes

Loss tangent (tan δ) calculated using the formula:

$$\tan\delta = \frac{\varepsilon^{''}}{\varepsilon^{'}} \qquad (2.16)$$

Also, ac conductivity can be obtained using dielectric constant and loss tangent using the following relation:

$$\sigma_{ac} = \varepsilon' \varepsilon_0 \omega \tan\delta \qquad (2.17)$$

Where $\omega = 2\pi f$

2.2.4 Magnetic Measurements

The number of available free electrons in the constituent atoms of a particular material decides its magnetic transport properties. It also depends on the exchange interactions i.e. the magnetic collaboration between the two neighboring magnetic atoms. The multiferroic nature of the material can be extracted by combining the magnetic properties with the electrical properties of the samples. Magnetic characterization includes the measurement of magnetization of the sample as a function of applied magnetic field and temperature.

2.2.4.1 Magnetization vs. Applied magnetic field (H)

Ferromagnetic materials can be understood by studying the hysteresis curve, which is a plot of the magnetization (M) vs. the applied magnetic field (H). Further such materials can be classified as hard magnetic materials and soft magnetic materials. Hard magnets are characterized by their requirement of ahigh magnetic field to magnetize and demagnetize, along with high energy loss. such materials in many applications including fractional horsepower motors, earphones, audio- and video- recorders, computer accessories, automobiles, and clocks.

Themagnetic hysteresis curve helpsus to find material-specific properties like the coercive field, remnant magnetization, and saturation magnetization. Also whether the material is paramagnetic, diamagnetic, ferromagnetic, etc. can be identified along with energy loss.

Different types of magnetic materials can be differentiated by the structure of magnetic dipoles in the regions known as domains. Each domain has a permanent net magnetic moment arising due to the alignment of the magnetic moments. The domains are separated by the Bolch walls which are the domain boundaries. These are narrow zones where the direction of the magnetic moment gradually and continuously changes from one domain to the next. The size of the domains is about 50 μm or less and the Bolch wall is about 100 nm thick. Each grain in a polycrystalline material may have more than one microscopic-sized domain.

The individual domains have random orientation in the absence of amagnetic field and such arrangement of domains shows the lowest free energy. The magnetic field-dependent magnetization for different types of magnetic materials is different. Such relationship for different types of magnetic materials is shown in the figure below:

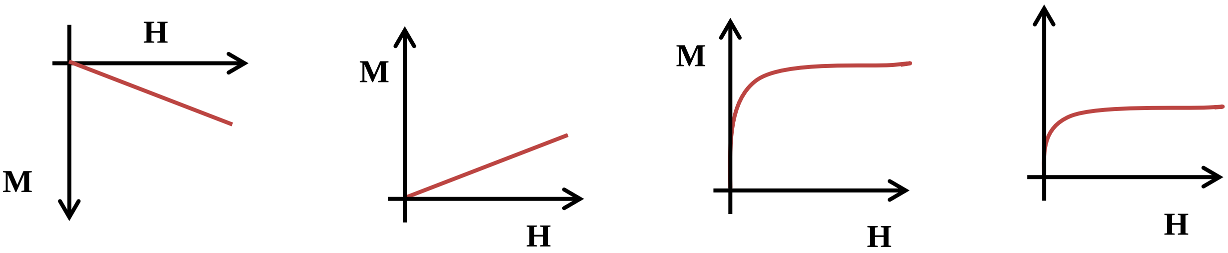

Diamagnetic Material
(a)

Paramagnetic Material
(b)

Ferromagnetic Material
(c)

Ferrimagnetic Material
(d)

Figure 2.18: Magnetization field (H) dependent magnetic diagrams for different types of magnetic materials

Diamagnetic materials: A diamagnetic material shows weak and non-permanent magnetism only in the presence of the magnetic field. The applied magnetic field unbalances the orbiting electrons of the constituent atoms of the material, which produces small magnetic dipoles which oppose the applied field. This creates a negative magnetic effect known **as** diamagnetism. Such materials show very small and negative magnetization as shown in figure (2.18 (a)).

Paramagnetic materials: Substances showing a small positive magnetic susceptibility (Figure 2.18 (b)) in the presence of amagnetic field are called paramagneticin nature, and the effect is termed as Para-magnetism. The presence of unpaired electrons gives rise to such behavior. The magnetic moment in such materials is zero in the absence of a magnetic field. But when the magnetic field is applied a small positive magnetization occurs. Also, large magnetic fields are required. An increase in temperature decreases the paramagnetic effect, as thermal agitation randomizes the direction of the magnetic dipoles.

Ferromagnetic Materials: Some substances possess permanent magnetic momentseven in the absence of an applied magnetic field. The magnetic dipoles of these substances easily align with the applied magnetic field through exchange interactions or mutual reinforcement of the dipoles. Ferromagnetic materials behave as para-magnetic above a particular temperature known as Curie temperature and their susceptibility is given by the Curie-Weiss law [50]:

$$\chi_m = \frac{C}{T - T_c} \qquad (2.18)$$

Where T = temperature, T_c = Curie temperature, C = material constant

Such materials are very strong magnets and magnetic dipoles align permanently upon the application of the external field (Figure 2.18 (c)).

Anti-Ferro-magnetic Materials: In such materials magnetic dipoles align in opposite directions, resulting in zero magnetization. Parallel alignment is a result of exchange interaction which is sensitive to atomic positions and inter-atomic spacing. Such an effect is responsible for anti-parallel alignment of spins. Quiet small susceptibilities are observed because of the equal strength of the anti-parallel spin magnetic moments. An important trait of anti-ferromagnetsis that they achieve maximum susceptibility at a critical temperature called Neel temperature. Above this temperatures they become Para-magnetic.

Ferri-magnetic materials: Some ceramic materials show ferri-magnetic behavior. Ferrimagnetism is similar to that of anti-ferromagnetism where the magnetic moments align antiparallel to each other. But they do not cancel each other out, and resulting in a spontaneous magnetization. The super-exchange behavior that occurs in oxide materials explains the antiparallel magnetic moments in both ferromagnetic and antiferromagnetic materials. Also, the net magnetic moment in such materials is less than in the ferromagnetic materials (Figure 2.18 (d)).

M-H hysteresis of Ferromagnetic materials:

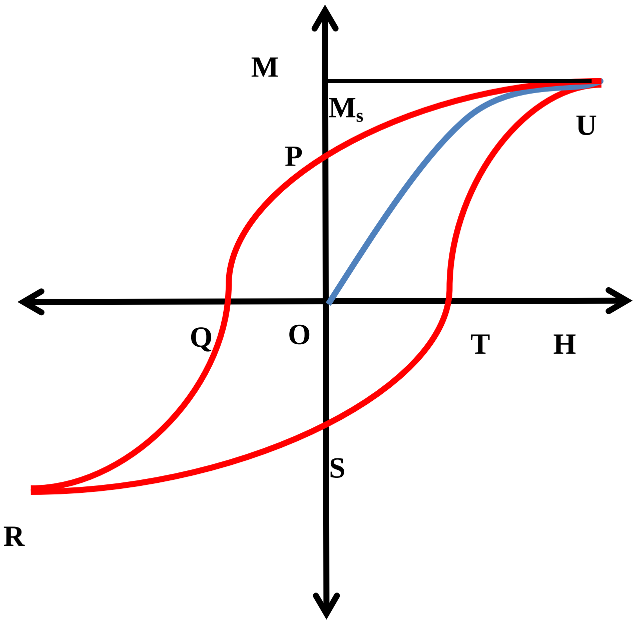

Figure 2.19: Hysteresis loop or M-H plot for typical ferromagnetic materials

Themagnetic behavior of ferromagnetic materials is represented by thehysteresis curve, which is a plot between magnetization and applied magnetic field. For a non-magnetic sample where the magnetic domains are randomly aligned M and H are zero. As the applied field isincreased the magnetization also increases and becomes saturated at very high applied fields as shown in fig. 2.19 (curve OU). This saturated value of magnetization is called saturation magnetization (M_s). a macroscopically permanent or residual magnetization isresulted even on the decrease of the applied field back to zero, such magnetization is known as remnant magnetization (M_r). Such effect of retardation shown by the material is known as hysteresis. The reversed magnetic field required to bring the remnant magnetization to zero is called Coercivity (curve OQ). Further increase in the reversed magnetic field results in a maximum induction in the opposite direction. Now the field can once again be reversed and theloop of field magnetization can be closed. Such a loop is known as hysteresis loop or M-H plot.

These type of studies helps in distinguishing the type of magnetism present in the sample. Based on the value of the Coercivity magnetic materials can be categorized as hard and soft magnets. The soft magnets are characterized by low coercive forces and high magnetic permeability. They are easily magnetized and demagnetized. Also, they exhibit small hysteresis losses. On the other hand, hard magnets have high coercive fields and high remnant inductions. They are also called permanent magnets. They exhibit large hysteresis losses.

In this study**,** M-H curve measurements were carried out using a **Squid magnetometer (Quantum Design) at the Department of Physics, National Dong Hwa University, Hualien, Taiwan**. The hysteresis curves were measured at three different temperatures 25 K, 40 K and 150 K.

2.2.4.2 Temperature and Field dependent Magnetization (M-T Curve)

A possible magnetic phase transition can be identified using temperature-dependent magnetizing curves. The thermal randomization due to the applied field is described by the Curie law, $\chi = C/T$ (where C = Curie constant and T = temperature in Kelvin) [50].

In paramagnetic substances, there are weakly interacting and localized electrons and they obey the Curie-Weiss law [50].

$$\chi_m = \frac{C}{T-\theta} \qquad (2.19)$$

χ_m = magnetic susceptibility

C = Curie constant

θ = Weiss Constant

A Curie-Weiss plot which is ($1/\chi_m$) vs temperature is known as the curie-Weiss plot. It should be linear if the C-W law is obeyed. The values of the Curie constant and Weiss constant values can be extracted from the slope and y-intercept of the graph.

In ferromagnetic substances, the magnetic moments of atoms align to produce **a** strong magnetic effect and the Curie law becomes:

$$\chi = \frac{C}{T-T_c} \qquad (2.20)$$

T_c = Curie temperature

Like ferromagnetism, the magnetic moments of atoms or molecules in antiferromagnetic materials are typically related to the spins of electrons, aligning in aregular pattern with the neighboring spins on different sublattices pointing in opposite directions. Such an alignment occurs at a temperature below a critical temperature known as Neel's Temperature. After

Neel’s temperature, the substance becomes paramagnetic. For anti-ferromagnetism the Curie Law becomes [50]:

$$\chi = \frac{C}{T+T_N} \qquad (2.21)$$

Typical χ vs T curves for para-, ferro- and anti-ferro magnetic materials are given below:

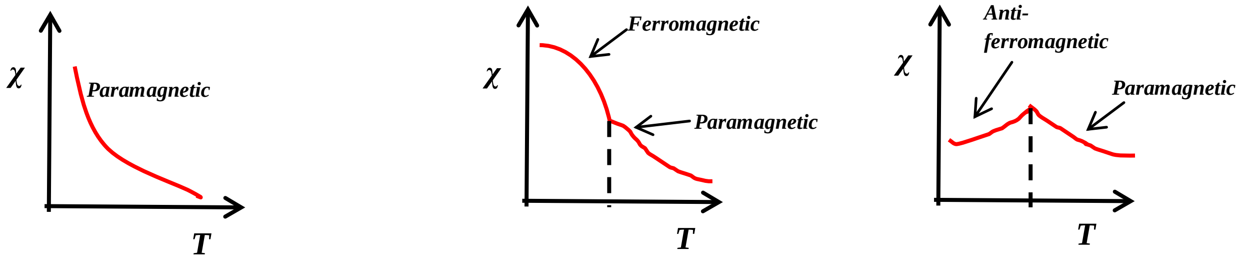

Figure 2.20: Magnetic susceptibility vs temperature (Kelvin) for paramagnetic, ferromagnetic, and antiferromagnetic materials

The application of the magnetizing field cannot alter the genuine phase transition, but the amount of magnetization does change and the history of the sample may change. Such facts make it possible to identify ferromagnetic and paramagnetic materials. In this experiment, measurements need to be performed under zero-field cooling (ZFC) and field cooled (FC) conditions.

In the present study**,** M-T curve measurements were carried out using **a Squid magnetometer (Quantum Design) at the Department of Physics, National Dong Hwa University, Hualien, Taiwan**. The M-T curves were measured between the temperatures of 5 K to 300 K.

References

[1] A. R. West, “SOLID STATE CHEMISTRY AND ITS APPLICATIONS.,” *Solid State Chem Its Appl*, 1984, doi: 10.1016/0254-0584(84)90072-5.

[2] Nishant Barot, P. K. Mehta, D. D. Shah, and C. J. Panchal, “Structure, I-V characteristics and optical studies of delafossite $CuFeO_2$and $CuFe_{0.96}Ti_{0.03}V_{0.01}O_2$ prepared under high vacuum,” in *AIP Conference Proceedings*, 2017, vol. 1837. doi: 10.1063/1.4982115.

[3] L. Amarande, C. Miclea, M. Cioangher, M. N. Grecu, and I. Pasuk, “Effects of vanadium doping on sintering conditions and functional properties of NbLi co-doped PZT ceramics. Comments on Li location,” *J. Alloys Compd.*, vol. 685, pp. 159–166, Nov. 2016, doi: 10.1016/J.JALLCOM.2016.05.266.

[4] B. D. (Bernard D. Cullity, “Elements of x-ray diffraction,” p. 555, 1978.

[5] M. A. Tagliente and M. Massaro, “Strain-driven (0 0 2) preferred orientation of ZnO nanoparticles in ion-implanted silica,” *Nucl. Instruments Methods Phys. Res. Sect. B Beam Interact. with Mater. Atoms*, vol. 266, no. 7, pp. 1055–1061, Apr. 2008, doi: 10.1016/j.nimb.2008.02.036.

[6] H. M. Rietveld, “A profile refinement method for nuclear and magnetic structures,” *J. Appl. Crystallogr.*, vol. 2, no. 2, pp. 65–71, 1969, doi: 10.1107/s0021889869006558.

[7] J. Rodríguez-Carvajal, “Introduction to the Program FULLPROF: Refinement of Crystal and Magnetic Structures from Powder and Single Crystal Data”.

[8] J. C. (John C. Taylor and I. Hinczak, *Rietveld made easy : a practical guide to the understanding of the method and successful phase quantifications*, 4th printing. Canberra: Sientronics, 2006.

[9] “scanning electron microscope | Definition, Images, Uses, Advantages, & Facts | Britannica.” https://www.britannica.com/technology/scanning-electron-microscope (accessed Mar. 13, 2022).

[10] A. Smekal, “Zur Quantentheorie der Dispersion,” *Naturwissenschaften 1923 1143*, vol. 11, no. 43, pp. 873–875, Oct. 1923, doi: 10.1007/BF01576902.

[11] C. V. Raman and K. S. Krishnan, “A new type of secondary radiation,” *Nature*, vol. 121, no. 3048, pp. 501–502, 1928, doi: 10.1038/121501c0.

[12] W. E. Modern Raman Spectroscopy-A Practical Approach, G. Smith, and Ó. Dent, “Modern raman spectroscopy: A practical approach,” *Mod. Raman Spectrosc. A Pract. Approach*, pp. 1–241, Jan. 2019, doi: 10.1002/0470011831.

[13] B. (Barbara H. . Stuart, “Infrared spectroscopy : fundamentals and applications,” p. 224, 2004.

[14] D. Peak, “FOURIER TRANSFORM INFRARED SPECTROSCOPY,” *Encycl. Soils Environ.*, vol. 4, pp. 80–85, Jan. 2005, doi: 10.1016/B0-12-348530-4/00174-0.

[15] R. L. Mössbauer, “Kernresonanzfluoreszenz von Gammastrahlung in Ir191,” *Zeitschrift für Phys. 1958 1512*, vol. 151, no. 2, pp. 124–143, Apr. 1958, doi: 10.1007/BF01344210.

[16] C. Sauer and W. Zinn, “Conversion Electron Mössbauer Spectroscopy Of Magnetic Multilayers,” *Magn. Multilayers*, pp. 147–181, Dec. 1994, doi: 10.1142/9789814447034_0006.

[17] H. Wegener, *Der Mössbauer-Effekt und seine Anwendungen in Physik und Chemie*, 2. erw. Aufl. Mannheim: Bibliographisches Institut, 1966.

[18] M. H. Cohen and F. Reif, “Quadrupole Effects in Nuclear Magnetic Resonance Studies of Solids,” *Solid State Phys. - Adv. Res. Appl.*, vol. 5, no. C, pp. 321–438, Jan. 1957, doi: 10.1016/S0081-1947(08)60105-8.

[19] Y.-L. C. and D.-P. Yang, *Mossbauer Effect in Lattice Dynamics*. 316AD.

[20] W. Marshall and C. E. Johnson, “Hyperfine field in metals and alloys,” *J. Phys. le Radium*, vol. 23, no. 10, pp. 733–737, Oct. 1962, doi: 10.1051/JPHYSRAD:019620023010073300.

[21] “Mössbauer Spectroscopy Group.” https://www.rsc.org/membership-and-community/connect-with-others/through-interests/interest-groups/mossbauer/ (accessed Mar. 13, 2022).

[22] F. Van Der Woude and G. A. Sawatzky, “Hyperfine magnetic fields at Fe^{57} nuclei in ferrimagnetic spinels,” *Phys. Rev. B*, vol. 4, no. 9, pp. 3159–3165, 1971, doi: 10.1103/PHYSREVB.4.3159.

[23] “Mössbauer spectra and magnetic properties of iron compounds — the University of

Groningen research portal.” https://research.rug.nl/en/publications/mössbauer-spectra-and-magnetic-properties-of-iron-compounds (accessed Mar. 13, 2022).

[24] F. van der Woude, “Mössbauer Effect in α-Fe_2O_3,” *Phys. status solidi*, vol. 17, no. 1, pp. 417–432, Jan. 1966, doi: 10.1002/PSSB.19660170147.

[25] G. J. Perlow, C. E. Johnson, and W. Marshall, “Mössbauer effect of Fe^{57} in a cobalt single crystal,” *Phys. Rev.*, vol. 140, no. 3A, 1965, doi: 10.1103/PHYSREV.140.A875.

[26] J. E. Miller and E. J. Sharp, “Optical Properties and Energy Transfer in LiYF4:Nd3+, Yb3+,” *J. Appl. Phys.*, vol. 41, no. 11, p. 4718, Dec. 2003, doi: 10.1063/1.1658520.

[27] E. J. Sharp and J. E. Miller, “Nonradiative Energy Transfer from Nd to Yb in a Crystal Ba2MgGe2O7,” *J. Appl. Phys.*, vol. 40, no. 11, p. 4680, Nov. 2003, doi: 10.1063/1.1657266.

[28] “Shodhganga@INFLIBNET: Structural and Magnetic Properties of Indium Substituted Nickel Zinc Ferrites Synthesized via Reverse Micelle Technique.” https://shodhganga.inflibnet.ac.in/handle/10603/11087 (accessed Mar. 13, 2022).

[29] “20200827110806_265333.png (1200×911).” https://csruserportal.com/facilities/20200827110806_265333.png (accessed Mar. 13, 2022).

[30] G. H. Haertling, “Ferroelectric Ceramics: History and Technology,” *J. Am. Ceram. Soc.*, vol. 82, no. 4, pp. 797–818, Apr. 1999, doi: 10.1111/J.1151-2916.1999.TB01840.X.

[31] L. Eric Cross, “Relaxor ferroelecirics,” *Ferroelectrics*, vol. 76, no. 1, pp. 241–267, 1987, doi: 10.1080/00150198708016945.

[32] S. Ke, H. Huang, and H. Fan, “Cite as,” *Appl. Phys. Lett*, vol. 89, p. 182904, 2006, doi: 10.1063/1.2374682.

[33] J. Liu, C. G. Duan, W. G. Yin, W. N. Mei, R. W. Smith, and J. R. Hardy, “Large dielectric constant and Maxwell-Wagner relaxation in Bi 2/3Cu3Ti4O12,” *Phys. Rev. B - Condens. Matter Mater. Phys.*, vol. 70, no. 14, p. 144106, Oct. 2004, doi: 10.1103/PHYSREVB.70.144106/FIGURES/11/MEDIUM.

[34] S. Saha and T. P. Sinha, “Structural and dielectric studies ofBaFe0.5Nb0.5O3,” *J. Phys.*

Condens. Matter, vol. 14, no. 2, p. 249, Dec. 2001, doi: 10.1088/0953-8984/14/2/311.

[35] D. C. Sinclair, T. B. Adams, and F. D. Morrison, “One-step internal barrier layer capacitor ARTICLES YOU MAY BE INTERESTED IN,” *Cite as Appl. Phys. Lett*, vol. 80, p. 2153, 2002, doi: 10.1063/1.1463211.

[36] Z. Wang, X. M. Chen, L. Ni, and X. Q. Liu, “Dielectric abnormities of complex perovskite Ba(Fe1⁄2Nb1⁄2)O3 ceramics over broad temperature and frequency range,” *Appl. Phys. Lett.*, vol. 90, no. 2, p. 022904, Jan. 2007, doi: 10.1063/1.2430939.

[37] I. P. Raevski, S. A. Prosandeev, A. S. Bogatin, M. A. Malitskaya, and L. Jastrabik, “High dielectric permittivity in AFe1/2B1/2O3 nonferroelectric perovskite ceramics (A=Ba, Sr, Ca; B=Nb, Ta, Sb),” *J. Appl. Phys.*, vol. 93, no. 7, p. 4130, Mar. 2003, doi: 10.1063/1.1558205.

[38] F. Zhao, Z. Yue, J. Pei, D. Yang, Z. Gui, and L. Li, “Dielectric abnormities in BaTi0.9(Ni1⁄2W1⁄2)0.1O3 giant dielectric constant ceramics,” *Appl. Phys. Lett.*, vol. 91, no. 5, p. 052903, Jul. 2007, doi: 10.1063/1.2767190.

[39] Ü. Özgür *et al.*, “A comprehensive review of ZnO materials and devices,” *J. Appl. Phys.*, vol. 98, no. 4, p. 041301, Aug. 2005, doi: 10.1063/1.1992666.

[40] D. M. Bagnall *et al.*, “Optically pumped lasing of ZnO at room temperature,” *Appl. Phys. Lett.*, vol. 70, no. 17, p. 2230, Jun. 1998, doi: 10.1063/1.118824.

[41] T. Aoki, Y. Hatanaka, and D. C. Look, “ZnO diode fabricated by excimer-laser doping,” *Appl. Phys. Lett.*, vol. 76, no. 22, p. 3257, May 2000, doi: 10.1063/1.126599.

[42] C. Boemare, T. Monteiro, M. J. Soares, J. G. Guilherme, and E. Alves, “Photoluminescence studies in ZnO samples,” *Phys. B Condens. Matter*, vol. 308–310, pp. 985–988, Dec. 2001, doi: 10.1016/S0921-4526(01)00854-7.

[43] U. Pal, D. Samanta, S. Ghorai, and A. K. Chaudhuri, “Optical constants of vacuum-evaporated polycrystalline cadmium selenide thin films,” *J. Appl. Phys.*, vol. 74, no. 10, p. 6368, Aug. 1998, doi: 10.1063/1.355161.

[44] D. G. Barton, M. Shtein, R. D. Wilson, S. L. Soled, and E. Iglesia, “Structure and Electronic Properties of Solid Acids Based on Tungsten Oxide Nanostructures,” *J. Phys. Chem. B*, vol. 103, no. 4, pp. 630–640, Jan. 1999, doi: 10.1021/JP983555D.

[45] P. Kubelka and F. Munk, “An Article on Optics of Paint Layers,” 1931.

[46] B. Kruse and L. Yang, “Revised Kubelka–Munk theory. I. Theory and application,” *JOSA A, Vol. 21, Issue 10, pp. 1933-1941*, vol. 21, no. 10, pp. 1933–1941, Oct. 2004, doi: 10.1364/JOSAA.21.001933.

[47] J. Torrent and V. Barrón, “DIFFUSE REFLECTANCE SPECTROSCOPY OF IRON OXIDES,” 2002.

[48] R. A. (Robert A. Smith, “Semiconductors,” p. 523, 1978.

[49] L. J. van der Pauw, “van der pauww.pdf,” *Philips Res. Reports*, vol. 13, p. 1, 1958.

[50] D. K. Schroder, “Electrochemical C-V Profiler,” *Semicond. Mater. device Charact.*, pp. 77–79, 2006, Accessed: Mar. 14, 2022. [Online]. Available: http://eu.wiley.com/WileyCDA/WileyTitle/productCd-0471739065.html

[51] B. D. CULLITY, “Introduction to magnetic materials -Cap 6 Ferrimagnetism,” pp. 175–195, 2009.